A&A 526, A137 (2011)
DOI: 10.1051/0004-6361/201015231

Astronomy & Astrophysics

A single picture for solar coronal outflows and radio noise storms

G. Del Zanna[1], G. Aulanier[2], K.-L. Klein[2], and T. Török[2]

[1] DAMTP, Centre for Mathematical Sciences, Wilberforce road, Cambridge CB3 0WA, UK
e-mail: g.del-zanna@damtp.cam.ac.uk
[2] LESIA, Observatoire de Paris, CNRS, UPMC, Université Paris Diderot, 5 place Jules Janssen, 92190 Meudon, France

Received 17 June 2010 / Accepted 27 September 2010

ABSTRACT

We propose a unified interpretation for persistent coronal outflows and metric radio noise storms, two phenomena typically observed in association with quiescent solar active regions. Our interpretation is based on multi-wavelength observations of two such regions as they crossed the meridian in May and July 2007. For both regions, we observe a persistent pattern of blue-shifted coronal emission in high-temperature lines with Hinode/EIS, and a radio noise storm with the Nançay Radioheliograph. The observations are supplemented by potential and linear force-free extrapolations of the photospheric magnetic field over large computational boxes, and by a detailed analysis of the coronal magnetic field topology. We find true separatrices in the coronal field and null points high in the corona, which are preferential locations for magnetic reconnection and electron acceleration. We suggest that the continuous growth of active regions maintains a steady reconnection across the separatrices at the null point. This interchange reconnection occurs between closed, high-density loops in the core of the active region and neighbouring open, low-density flux tubes. Thus, the reconnection creates strong pressure imbalances which are the main drivers of plasma upflows. Furthermore, the acceleration of low-energy electrons in the interchange reconnection region sustains the radio noise storm in the closed loop areas, as well as weak type III emission along the open field lines. For both active regions studied, we find a remarkable agreement between the observed places of persistent coronal outflows and radio noise storms with their locations as predicted by our interpretation.

Key words. Sun: corona – Sun: radio radiation – techniques: spectroscopic

1. Introduction

Solar active regions (ARs) are composed of a multitude of coronal loops with different temperatures and sizes, emitting mainly in EUV and X-rays. They consist of hot (2–3 MK) small-scale loops in their cores, and "warm" (1 MK) large-scale loops around them. Loops of different temperatures are normally persistent and intermingled, as seen with SOHO/CDS observations (Del Zanna et al. 2006). Most of the 2–3 MK emission appears diffuse (Del Zanna & Mason 2003), i.e., still unresolved at the best EUV spatial resolution available to date (TRACE, 1″). In this paper, we study AR "quiescent" coronal emission which typically lasts for days. There are many outstanding open questions related to AR loops. In recent years, more unexplained features have been observed, in particular plasma flows in the corona. EUV imaging by TRACE has shown ubiquitous apparent coronal upflows in warm large-scale loops (e.g. Schrijver et al. 1999; Winebarger et al. 2001). EUV spectroscopy with SOHO/SUMER on the other hand showed redshifts in the profiles of lines formed at transition region temperatures (e.g. Ne VIII, see Winebarger et al. 2002).

Dopplershifts in spectral lines have been observed by a wide range of spectroscopic instruments in the past, but it was not until the launch of Hinode that a clear pattern of Dopplershifts in coronal lines was observed with the EUV Imaging Spectrometer (EIS, see Culhane et al. 2007). Its high spectral resolution allows EIS to measure Dopplershifts with an accuracy of a few km s^{-1} in coronal lines formed between 0.7 and 3 MK, which were difficult to observe with previous instruments. EIS observations have confirmed and extended the SUMER results: Del Zanna (2007, 2008b) showed that persistent redshifts, stronger in cooler lines, are typically observed at both footpoints of most AR loops. This emission appears to be due to plasma that is slowly radiatively cooling as it flows down. It is still unclear, however, why the chromospheric evaporation that must replenish the coronal loops has not yet been observed.

An interesting discovery made by EIS was the existence of persistent blue-shifted emission in coronal lines, commonly interpreted as a signature of *coronal outflow*. Using EIS data together with magnetograms from Hinode/SOT, Del Zanna (2007, 2008b) showed that this blue-shifted emission is: a) progressively larger in lines formed at $T > 1$ MK; b) located exactly above regions of strong magnetic field (sunspots umbrae and plage); c) originating at low heights, but with a large spatial expansion into the corona; d) located in regions where typical electron densities are two orders of magnitude smaller than the typical densities (10^9 cm^{-3}) of the hot loops in the core; e) associated with large (>50 km s^{-1}) non-thermal broadenings in the line profiles; f) persistent and unchanged in strength over a relatively long period of time (days). These results pertained to NOAA 10926, but turned out to be quite general. Similar results on other ARs have been found (see, e.g. Del Zanna & Bradshaw 2009; Doschek et al. 2008; Hara et al. 2008; Baker et al. 2009).

The origin of these coronal outflows is still unclear. Del Zanna (2008b) suggested that they could be due to chromospheric evaporation following magnetic reconnection, based on their morphological similarities with the well-known upflows associated with solar flares. Various authors have suggested that the coronal outflows could be related to the origin of the slow solar wind. For example, Marsch et al. (2008) considered the same EIS observations as presented in Del Zanna (2008b) and found

that the blue-shifts were associated with regions where the extrapolated coronal field lines appeared open. Similar suggestions were made by Harra et al. (2008) and Doschek et al. (2008).

Baker et al. (2009) presented Hinode/EIS observations of NOAA 10942 and supplemented them with detailed magnetic field modelling. They found that the coronal outflow regions were associated with regions where the extrapolated field lines showed a rapid change in connectivity, namely quasi-separatrix layers (QSLs; e.g., Demoulin et al. 1996). The authors listed several outflow mechanisms related to magnetic reconnection occurring at QSLs. Based on a comparison of an MHD simulation with observations of a small AR surrounded by a coronal hole (CH) on 17 October 2007, Murray et al. (2010) suggested that coronal outflows are driven, at least partially, by thermal pressure gradients which develop in the magnetic field surrounding an AR, due to the deformation of these fields by the continuous expansion of the AR.

In this paper we explore the relation between coronal outflows and one other well-known, but still largely unexplained solar phenomenon that requires a quasi-continuous energy release over several days in a non-flaring active region, namely *radio noise storms*. Noise storms are broadband emissions lasting for hours or days at frequencies between roughly 100 and 500 MHz. They are associated with active regions, but not directly with flares (for reviews, see Elgarøy 1977; Kai et al. 1985; Klein 1998). Noise storm observations were presented by, e.g., Krucker et al. (1995) and Malik & Mercier (1996), and their relationship to evolving magnetic structures in the solar atmosphere was discussed in Stewart et al. (1986), Raulin & Klein (1994), Bentley et al. (2000), and Willson (2005).

Noise storm emission has a characteristically strong circular polarisation, ascribed to emission at the electron plasma frequency, and brightness temperatures that may exceed coronal electron temperatures by several orders of magnitude (Kerdraon & Mercier 1983). It is therefore attributed to non-thermal electrons whose energy is not well known, but was estimated to be about 10 keV, from considerations of collisional lifetimes of the emitting electrons and from broadband fluctuations of the noise storm continuum emission (Raulin & Klein 1994). The lifetime of such electrons in an ambient medium of an electron density corresponding to the range of emission frequencies quoted above, i.e. roughly 10^8–10^9 cm^{-3}, does not exceed a few tens of seconds. Hence electrons must be accelerated throughout the whole duration of the noise storm emission. This is different to flares, which are in general related to particle acceleration over only rather short durations. The rate of energy release in noise storms estimated from these considerations is about 10^{23}–10^{25} erg s^{-1} (Raulin & Klein 1994), and a similar range was derived from theoretical investigations of stochastic electron acceleration by Subramanian & Becker (2004).

At their low-frequency end, noise storms are often accompanied by storms of decametric-to-kilometric type III bursts (Kai et al. 1985; Kayser et al. 1987). These are short (second duration) bursts emitted by electron beams rising through the corona. The beam-plasma instability creates Langmuir waves at the local electron plasma frequency, which can be converted into electromagnetic waves near the electron plasma frequency or its harmonic. The result is a short emission in the radio spectrum that drifts from high to low frequencies as the electron beams proceed to greater altitudes. Numerous type III bursts at the low-frequency side of metre wave noise storms confirm the repeated acceleration of electrons in the corona over extended durations. Furthermore they indicate that the acceleration region of the electrons in the corona is magnetically connected to open field lines reaching into the high corona and interplanetary space.

The main aim of this paper is to present a possible explanation for the origin of the coronal outflows, and to link the related physical mechanism with radio noise storms. This is done by combining detailed observations and magnetic field modelling of two well-observed active regions.

2. Data analysis and modelling

We have extensively searched the entire Hinode database[1] for suitable AR observations. Our main criterion was that a sufficient number of observations were made during the meridian passage of quiescent ARs. We preferred small ARs, since they are more likely to fit into the typically small fields of view (FOV) of the Hinode instruments. Indeed, one important issue for EIS observations is the need to have a large FOV with respect to the AR size, in order to correct for instrumental wavelength shifts (although a new method has recently been suggested by Kamio et al. 2010) and to have a region which can be selected as reference for the wavelengths, as described below. We found and analysed a few ARs which fitted these criteria, but here present results pertaining to NOAA 10961 and NOAA 10955.

We note that many (if not all) ARs, for which blue-shifted emission at their edges have been recorded by EIS, appear to be surrounded by CHs, or at least by extended unipolar areas of the LOS magnetic field. This is also the case for the ARs studied here, and it is important for our interpretation of the origin of such blue-shifts, as we discuss below.

2.1. EIS

The EIS data were processed using custom-written software (see, e.g., Del Zanna 2008b,a). The offset between the SW and LW channels in both N-S (18″) and $E-W$ (2″) was corrected for. Some authors have recently found asymmetries in the EIS line profiles, which would question the use of single Gaussian profiles. Hara et al. (2008) found evidence for blue-wing asymmetries in the profiles of 2–3 MK lines (Fe XIV, Fe XV) in the blue-shifted regions of AR 10938. Recently, Peter (2010) reanalysed the same Fe XV observations and confirmed the presence of a double component. Bryans et al. (2010), on the other hand, presented observations of another AR, where strong asymmetries were only found in lines formed at 1 MK and *not* in 2–3 MK lines. The same authors report that lines from ions formed at 2–3 MK showed small outflow velocities comparable to those of the primary component of the cooler lines, however the intensities were too weak to accurately determine the shape of the profiles. De Pontieu et al. (2009) found an asymmetry in the blue wing of the Hinode EIS Fe XIV 274 Å line at the edges of NOAA 10976 and 10977 observed near disk center on 2007 December 2 and 5. The asymmetry is indicative of upflows of 50–100 km s^{-1} which are correlated with type-II spicules.

We have found no significant evidence for asymmetries in the line profiles. However, Doppler-shifts could only be measured in a few of the stronger lines, the best measurements being from the strongest Fe XII 195.12 Å self-blend. This is caused by low count rates in most lines, and by the fact that most EIS observations have been made with the 1″ slit and with short exposure times (to limit the duration of each observation). The *cfit* package (Haugan 1997) was used to fit Gaussian profiles to all the

[1] http://sdc.uio.no/search/API

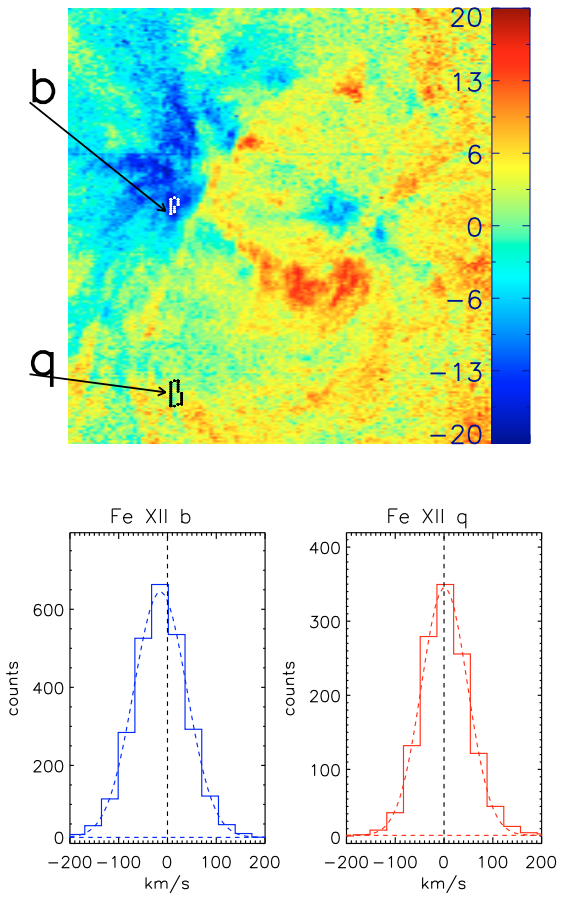

Fig. 1. Above: Dopplermap in Fe XII 195.119 Å (±20 km s^{-1}) of AR 10961 on 1 July 2007, with two selected regions, one within the coronal outflows (b), and one far from them (q). Below: Fe XII 195.119 Å line profiles in the selected regions, with superimposed Gaussian fitted profiles.

lines observed, using custom-written programs to obtain intensity, position and width.

Figure 1 shows one example from an observation of AR 10961 on 1 July 2007. Two regions were selected, one within the coronal outflows (b), and one far from them (q). The two regions were observed at the same time so the same wavelength shifts apply to them. The spectrum from region q was wavelength-calibrated so the Fe XII 195.119 Å line position is at rest wavelength. The line profile is Gaussian, with a full-width-half-maximum (*FWHM*) of 72 mÅ. The line widths in the EIS spectrometer are mostly instrumental. In the SW channel, where the Fe XII 195.119 Å line is located, the instrumental width is fairly constant in the bottom part of the slit, and then increases linearly with the position along the slit (details will be published elsewhere). In the quiet Sun, the *FWHM* in the central part of the slit is about 67 mÅ for most of the unblended lines, and 70 mÅ for the strong Fe XII 195.119 Å line. Therefore, the line profile in the q region is very similar to that one from the quiet Sun. The line profile b from the coronal outflow region is also very symmetric and Gaussian, with a centroid shifted towards the blue, and a larger *FWHM* of 83 mÅ.

A strong (75 km s^{-1}) orbital variation of the EIS wavelength scale is present. This variation is non-reproducible and wavelength-dependent. We have corrected for it by obtaining an average time-dependent wavelength scale for the two channels, using the brightest lines and the standard wavelength-to-pixel calibration. A further problem is that the *absolute* values of the Dopplershifts are quite uncertain. EIS is capable of measuring relative Dopplershifts with an accuracy of a few km^{-1}, but it does not have, or measure, "rest" wavelengths, so these can only be obtained by choosing a reference area (to which all velocities are relative to). The EIS measurements discussed in Del Zanna (2008b) are still the best case presented so far, since the instrument slit *rastered* a large FOV that contained quiet Sun areas, which were used as reference area for the rest wavelengths. In the observations presented here, wavelengths at rest were obtained from regions as far away as possible from the ARs' loop structures.

The co-alignment of each EIS raster was done by cross-correlating the monochromatic images in cooler lines with TRACE 171 Å images, whenever available. The co-alignment is very accurate (1–2″). However, the fast jitter of the EIS instrument while it scans means that locations of EIS features can only be obtained with an accuracy of 3–4″, which is the effective instrument resolution.

2.2. Other instruments

We have considered Hinode Solar Optical Telescope (SOT) Narrow-band Filter Imager (NFI) FG and the Spectropolarimeter (SP) data. The FG data were processed using the standard processing routine FG_PREP available within SolarSoft. The FG Stokes *V* images provide information on the line-of-sight magnetic field density with a resolution of about 0.16″. The SOT has an internal mechanism which tracks solar features. Despite this, a considerable "jitter" of a few arcseconds over short (minutes) time-scales is still present in both the SP and FG data. The jitter and pointing in the FG data was established by cross-correlating FG V images with simultaneous full-disk SOHO/MDI line-of-sight (LOS) magnetograms (which are taken every 96 min). For the SP, we have used the data processed in the standard way within SolarSoft. The results provide maps of the apparent longitudinal and transverse magnetic field density.

The Hinode XRT optics provide an excellent resolution of about 2″ (Golub et al. 2007). The data were processed using the standard software (XRT_PREP). The pointing of the full-disk images was obtained by fitting the visible limb, while the pointing of partial-frame data was obtained by cross-correlating with the full-disk images.

The TRACE instrument provides high-cadence images with the highest spatial resolution (1″) in three EUV bands, together with UV ones and the visible (white light) continuum. The images were processed using the standard SolarSoft routine EIS_PREP. The pointing of the TRACE images was obtained by cross-correlating the white light continuum with full-disk SOHO MDI data.

Radio images of the corona were taken at several frequencies between 150 and 432 MHz (wavelengths 0.69-2 m) by the Nançay Radioheliograph (henceforth referred to as NRH; Kerdraon & Delouis 1997). The observations are acquired with sub-second time resolution, but for the present study we used 10 s averaged values. Spectral observations with the Nançay Decameter Array (20–70 MHz, Lecacheux 2000) are used to identify the radiation of electron beams escaping to the high corona.

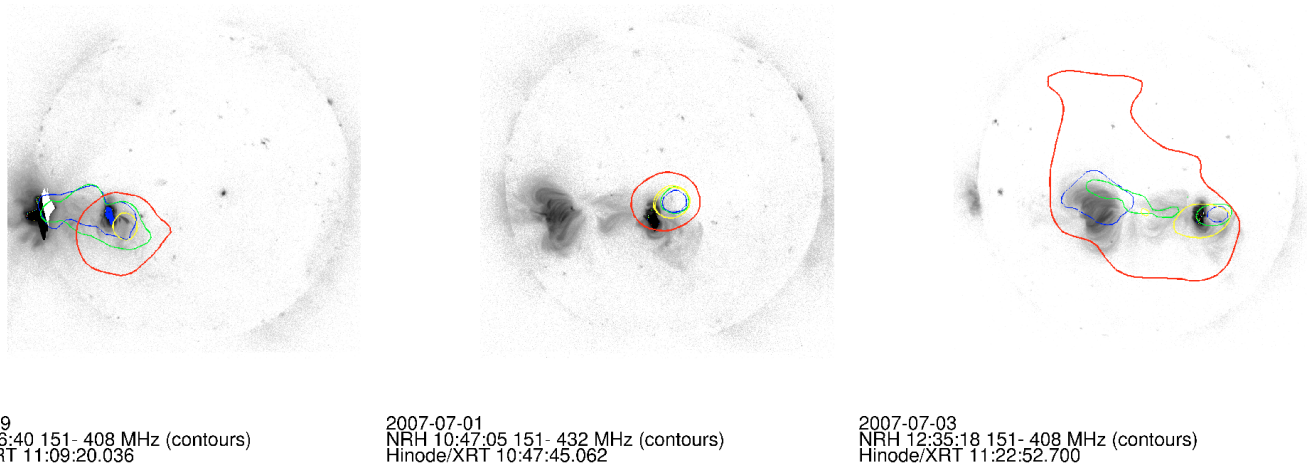

Fig. 2. X-ray (negative) images of the full Sun from Hinode XRT on 29 June, 1 July, and 3 July 2007. AR 10961 crossed the meridian on 1 July. Superimposed are contours of the radio sources at 408 (blue), 327 (green), 237 (yellow) and 151 MHz (red) (iso-intensity contours at 80% of the maximum, 5 min integration for 29 June and 3 July, 10 s on 1 July). The times of the radio images were chosen such as to give a typical view of the sources during these days, and differ from the times of the XRT images. Solar north is at the top, west on the right.

2.3. Magnetic field extrapolations

To obtain information on the magnetic connectivity above and around the studied ARs, we performed potential and linear force-free (lfff) magnetic field extrapolations. We used the BLFFF Cartesian code (Demoulin et al. 1996) from the FRench Online MAGnetic Extrapolations (FROMAGE) service[2], which is based on the FFT method (Alissandrakis 1981). Since the magnetic field data from Hinode/SOT are spatially too limited, given that ARs are typically magnetically connected to nearby CHs or other ARs, we used SOHO/MDI data for the extrapolations.

Taking into account the projection effects for the ARs, which were both located slightly offset to the solar disc centre, the coronal magnetic field $\boldsymbol{B}$ was computed from the photosphere up to an altitude $z = H$, using $B_z(z = 0) = B_{\|} \cos\psi$ as photospheric boundary condition. Here, $B_{\|}$ is the LOS magnetic field, where only a partial section of size $L_x \times L_y$ of the full-disc magnetogram was retained, and ψ is the angle between the z axis and the radial direction at the disc centre.

To minimize aliasing effects resulting from the periodic boundary conditions along the x and y directions, the deprojected SOHO/MDI magnetograms were inserted into wider regions of size D^2 Mm^2 with $B_z(z = 0) = 0$. The total $B_z(z = 0)$ was then developed into Fourier eigenmodes, with a resolution of 1024×1024. Using $\nabla \times \boldsymbol{B} = \alpha \boldsymbol{B}$, $B_{x,y}(z = 0)$ and $\boldsymbol{B}(z > 0)$ were calculated for a constant value of the force-free parameter α, which has (maximum and minimum) resonant values $\alpha_M = \pm 2\pi/D$. Potential fields correspond to $\alpha = 0$. The output vector field $\boldsymbol{B}$ was written on a mesh with a uniform spacing of 11 Mm in the x and y directions, and a non-uniform spacing in the z direction, with the smallest intervals of 2 Mm located close to $z = 0$.

To go a step beyond the similar analyses performed by Baker et al. (2009), where the small photospheric field area used for the extrapolation contained only one footpoint of the large-scale connections of the studied AR, we chose here L_x and L_y to be much larger than the AR size. This permits to calculate field lines that connect to neighbouring ARs, and therefore to distinguish them from field lines which leave the Sun towards the heliosphere, along which the solar wind can flow.

[2] http://www.solaire.obspm.fr/fromage/

3. NOAA 10961

NOAA 10961 appeared at the eastern limb on 25 June 2007 and crossed the meridian on 1 July. It was one of the "classical" ARs, with a sunspot as leading polarity and a scattered following polarity. The AR was very quiescent during meridian passage, in that only 2 B-class flares were observed between 30 June and 7 Jul. (when it reached the western limb). A larger number of B-class flares occurred before 30 June. To the east of NOAA 10961, a very large dispersed AR was present (NOAA 10962). Both active regions were not present during the previous solar rotation.

Figure 2 shows X-ray images of the full Sun from Hinode/XRT and radio emission contours from NRH. The X-ray images clearly show loops interconnecting the eastern polarities of AR 10961 with the western ones of AR 10962 (see also Fig. 5 below), indicating that the two ARs were magnetically connected.

AR 10961 is surrounded by CHs. While this is not evident in the negative XRT images in Fig. 6, it can be seen clearly in the XRT frame in Fig. 5a: a very dark CH is present to the west of AR 10961. There is also a dim region to the north-west of AR 10962, which could also be a CH, as suggested by the open field lines found at that location in the extrapolation (see Sect. 3.3 and Figs. 5b,c below).

3.1. Radio noise storm

On 1 July 2007, NRH observed a noise storm at all frequencies on top of the quiet coronal bremsstrahlung emission (Fig. 2). A single noise storm source was seen during the entire observing time (09–15 UT). The iso-intensity contours at 80% of maximum brightness are overplotted for all observed frequencies onto the Hinode/XRT images. The noise storm on 1 July appears to be related to the leading part of AR 10961.

The noise storm is less prominent, or even invisible, the days before and after 1 July. The irregular or extended contours on 29 and 30 June show that the noise storm is not much more intense than the bremsstrahlung emission from the quiet corona. The overplot of the radio sources on the Hinode/XRT image (Fig. 2, left) shows that the western noise storm is near the leading edge of the western AR 10962. The eastern component projects to the

trailing part of AR 10961, perhaps also on the leading part of AR 10962 (but the radio source does not extend sufficiently far above the limb to be sure of the latter).

At low frequencies, noise storm emission is visible sporadically (e.g., around 10:30–11:00 on 29 June, close to 09:40 UT on 30 June; at 151 MHz), but it is clearly not as sustained as on 1 July. The situation is similar on 2 and 3 July: occasional brightenings at low frequencies, extended emission at higher frequencies. As seen in Fig. 2 (right panel), emission at 408, 327, and 237 MHz now comes from both active regions. The large extent of the contour at 80% of maximum brightness at 151 MHz refers to thermal emission, because the noise storm source hardly, if at all, exceeds the quiet coronal radio emission.

In summary, NRH observed a slowly evolving noise storm above AR 10961 during its disk passage between June 29 and July 3 2007, with the most intense emission on 1 July. At frequencies below 100 MHz, the Nançay Decameter Array saw recurrent type III bursts and groups of type III bursts[3].

3.2. Multi-wavelength observations

Figure 3 shows a combination of various observations of AR 10961 around 15:00 UT on 1 July, when the AR was close to Sun centre. The SOT/SP data clearly show the presence of a nearly unipolar, radial magnetic field in the sunspot and plage regions. Large warm (1 MK) loops, whose legs are clearly visible in TRACE 171 Å and EIS Fe VIII emission, are connected with these regions. The hottest (3–5 MK) loops, clearly visible in the EIS Fe XV emission and in the XRT image, are located in the core and also connect the sunspot penumbra with the plage regions. Strong blue-shifts in lines formed above 1 MK are located within the sunspot and on a sharp boundary located in the plage. This is shown in Fig. 3 by the Doppler image in Fe XII, but all lines formed at the same or higher temperature showed similar characteristics.

The blueshifts within the plage regions are a new feature observed with Hinode (Del Zanna 2007, 2008b), however blue-shifts within sunspots have been observed before. There is an extensive literature on measurements of doppler-shifts within Sunspots, with (apparently) contradicting results. Brueckner (1981) found small (2.5 km s^{-1} on average) blue-shifts above a sunspot in Fe XII, from an excellent NRL/HRTS rocket spectrum. Chromospheric lines were used as reference for the wavelengths. Gurman & Athay (1983) also reported very small (1.2 km s^{-1} on average) blueshifts in C IV above sunspots as observed with SMM/UVSP, however the measurements were relative to a region of quiet Sun, where C IV is known to be red-shifted by about 4 km s^{-1}. Most other authors found redshifts within sunspots, which are probably caused by the dominance of the bright sunspot plumes, which are known to be strongly red-shifted. The first clear picture emerged from SOHO/SUMER raster observations, which have shown a clear pattern of progressively larger (in terms of area and strength) blue-shifts just above sunspots in transition-region lines formed at higher temperatures (see, e.g., Brynildsen et al. 1998; Marsch et al. 2004). The SUMER lines were formed from the chromosphere to the upper transition region (Ne VIII).

The new Hinode EIS and SOT observations clearly showed that the blue-shifts within the sunspots in NOAA 10926 extended in lines formed at 1 MK and above (Del Zanna 2007, 2008b). This was confirmed by Marsch et al. (2008), who actually analysed the same active region and used SOHO/ MDI data

[3] See http://secchirh.obspm.fr/index.php

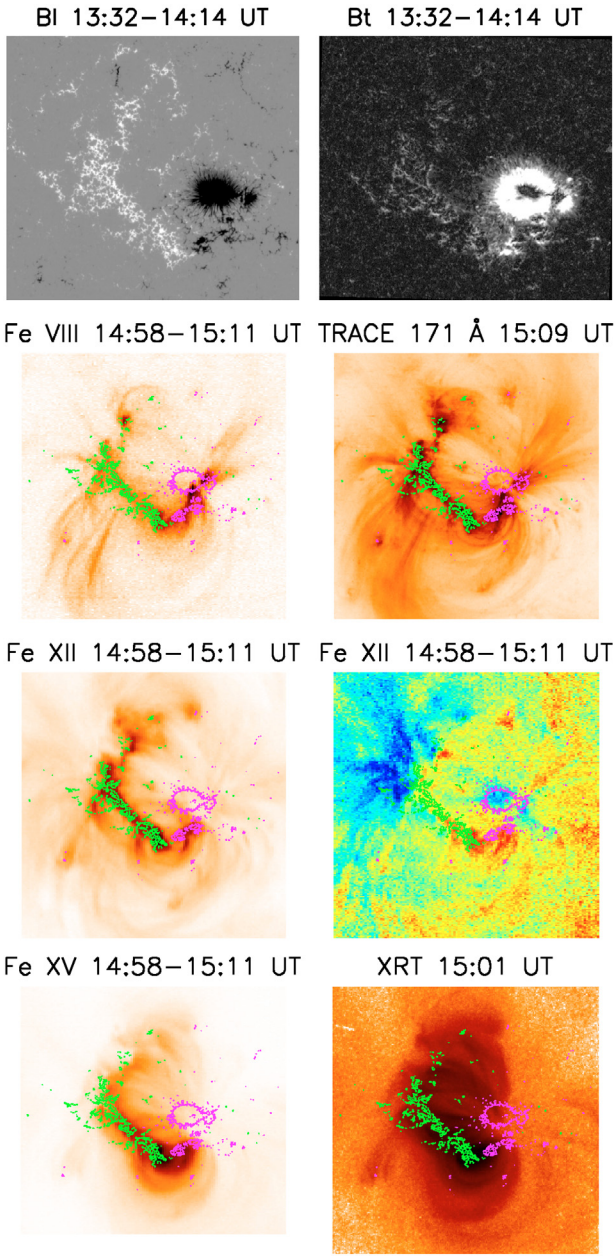

Fig. 3. AR 10961 on 1 July 2007. *Top to bottom*: longitudinal (±800 Gauss) and transverse (±500 Gauss) apparent magnetic field from SOT/SP; "cool" emission as seen in EIS Fe VIII and TRACE 171 Å; 1 MK emission as seen in EIS Fe XII, and associated Doppler-map (±30 km s^{-1}); "hot" emission as seen in EIS Fe XV and in XRT (Open + Ti-Poly). Contours superimposed on the images are from co-aligned SOT/FG data.

to locate one sunspot. On the contrary, Doschek et al. (2008) found blue-shifted plasma to be offset from the position of the sunspot in NOAA 10978.

For this paper, the interesting feature is that the blue-shifts are only observed on the north-eastern part of the plage, where actually "moss" emission is not very prominent. We will return to this point in Sect. 3.4.

Most of Hinode EIS observations of AR 10961 had a small FOV or low count rates, but some useful data are available from 29 June to 5 July. Figure 4 shows the persistence of the blue-shifts, mostly in the eastern side, during the course of at least 7 days, which is significant. The strongest Fe XIII line was used

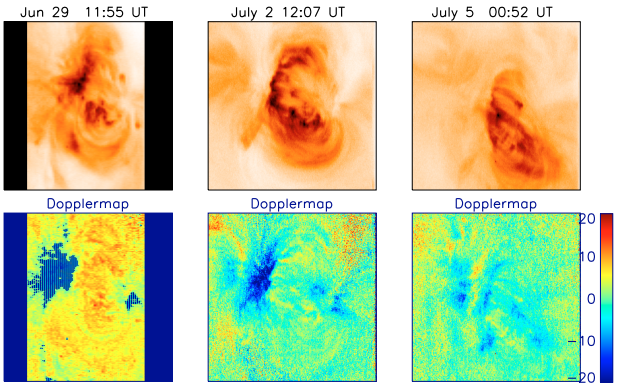

Fig. 4. AR 10961 from 29 June to 5 July 2007, as seen in Fe XIII monochromatic images (negative, *left*) and Dopplermaps (±20 km s^{-1}, *right*).

for these plots. The observation on 29 June was made with a "sparse raster" (when successive exposures are taken by moving the pointing by more than the slit width) having a smaller FOV (177″ in the east-west direction). The data gaps were filled by interpolation.

3.3. Magnetic field topology

The magnetic field extrapolation of AR 10961 and its surroundings was performed by employing SOHO/MDI magnetic data from 1 July 2007. The field was calculated up to $H = 2\ R_\odot$, using an MDI FOV of $L_x \times L_y = 1020'' \times 700''$, embedded in a $D = 2500$ Mm $\times 2500$ Mm zero-field region. The very large D value was required to minimize the otherwise strong aliasing effects in this complex and extended solar region, which comprised the remnants of AR 10962. This led us to perform a simple potential field extrapolation for this region, since such a large D implies a very small α_M value (see Sect. 2.3). The overall good match between the resulting magnetic field lines and the HINODE/XRT large-scale loops (see Figs. 5a,c) suggests that, at this length scales, the potential field approximation was acceptable (even though XRT and EIS loop observations suggest the presence of some magnetic shear inside AR 10961).

Figures 5b,c show a projection view and an observer's view on representative potential field lines in and around ARs 10961 and 10962. Internal active region field lines and interconnecting loops (IL) are drawn in yellow and green, respectively. Large field lines that leave the computational box, i.e. that are presumably open, are drawn in cyan (labelled CH E and CH W for the eastern and western CHs, respectively; they also correspond to dark regions as observed by XRT).

The separatrix field lines emanating from the null point are drawn in pink: there is a singular spine field line that is rooted on one of its sides within AR 10961, namely in the ARs leading negative polarity. On its other side, it is rooted in the dispersed negative polarity of AR 10962, eastwards of the ILs and just westwards from the footpoints of the CH E open field lines.

The lower part of the fan separatrix surface maps the C-shaped trailing eastern positive flux concentration of AR 10961, while its upper part is open. The topology of this null point configuration, embedded in a set of open field lines, does therefore not correspond to the typical configuration with an open spine (see, e.g., Pariat et al. 2009), but rather to that of a separatrix wall (as found by Priest et al. 1997, using magnetic source models). The projected locations of the uppermost parts of the open and diverging fan field lines (to the north and the west of AR 10961) correspond well to the locations of the brightest sources of the long-duration radio noise storm (compare Figs. 5c and 2).

We note that, in spite of the apparent quasi-2D quadrupolar distribution of flux of the two ARs along the east-west direction, the magnetic field topology is far from that of the "textbook" quadrupolar configuration, consisting of two closed (quasi-)separatrices that cross each other at some x-point (or x-line) in the corona. This difference is due to the existence of (the CH E and CH W) open field lines, which, in turn, exist due to a strong flux imbalance (negative) in the extrapolated region.

3.4. Interchange reconnection

As can be seen from MDI sequences (not shown), the photospheric area covered by AR 10961 increases during its gradual emergence and later decay, as it is the case for most solar active regions. According to magnetostatics, the outer field lines of the AR should quasi-statically bulge upwards, as a result of their slow footpoint separation. It is therefore likely that these field lines (yellow in the extrapolation; Figs. 5b,c) continuously reconnect with ambient field lines located on the other side of the separatrix of the null point. In the extrapolation, these ambient field lines are the open CH E field lines (cyan). The extrapolation therefore suggests that this interchange reconnection produces new IL closed field lines (green), and new CH W open field lines (cyan).

Selected field lines, located just at the edge of the separatrix, are drawn in Fig. 5d. They illustrate that the interchange reconnection between the AR (closed green lines) and CH E (open blue lines) involves only the central part of the northern section of the C-shaped plage region of AR 10961. Indeed, none of the thin blue field lines which can reconnect with the thin green lines emanating from its southern section and from its northern edge, are open (see Fig. 5d); all these (thin) field lines are closed and confined to low altitudes below two coronal pressure scale heights (i.e. below 100 Mm). This implies that they should not have such a low density as their neighbouring open field lines, an important point to which we will come back in Sects. 4.4 and 5.

In conclusion, the extrapolation suggests that the footpoints of the new field lines that result from interchange reconnection at the null point are located: (1) at the eastern edge of the northern part of the C-shaped plage region of the AR (see the red closed field lines in Fig. 5d, and (2) inside the leading negative polarity sunspot of the AR (see the pink open field lines in Fig. 5d). These two locations correspond exactly to those where persistent blueshifts are observed with EIS (see Figs. 3 and 4, and Sect. 3.2).

4. AR 10955

AR 10955 was a small AR that crossed the meridian on 11 May 2007 (see Fig. 6). It was relatively isolated, with only a small ephemeral region (ER) to its north-east, which displayed a bipolar magnetic pattern similar to the AR. Some emission in the X-rays indicates the presence of weak loops connecting AR 10955 with the ER. Hinode/EIS observations are available only from meridian passage until the region reached the western limb. Similar to AR 10961, also AR 10955 appears to be surrounded by regions of open field. Although clear indications of CHs can not be seen in the EUV and X-ray observations, the extrapolation presented below indicates the presence of open fields in the AR's vicinity.

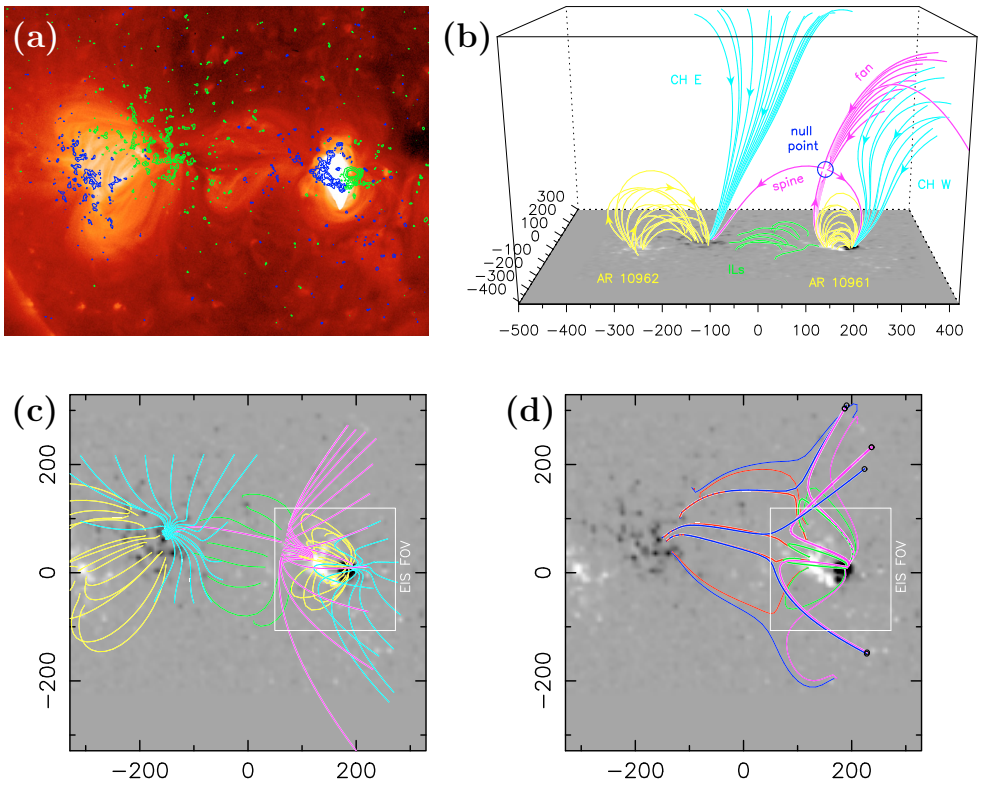

Fig. 5. **a)** X-ray image of AR 10961 from Hinode/XRT on 1 July 2007. Contours of the LOS magnetic field from SOHO/MDI are overlayed. **b–c)** Side and top view on selected field magnetic lines from the potential field extrapolation of the AR, outlining its main topological features (see text for details). **d)** Top view on selected field lines from the extrapolation, outlining the interchange reconnection between closed and open fields (see text for details). Open field lines are marked with a circle where they leave the computational box. The Hinode/EIS FOV is indicated in **c)** and **d)**.

4.1. Radio noise storm

On 12 May 2007 NRH observed a decaying, weak noise storm at high frequencies (327, 408, 432 MHz) during the whole observing period of that day (9–15 UT). At 242 MHz the noise storm was also observed, but clearly faded systematically during the day. At 151 MHz the fading was more pronounced, and the noise storm became undetectable before 12 UT.

Figure 6 shows the radio positions superimposed on Hinode/XRT images around meridian passage. In order to display the noise storm sources of 12 May, contours at 80% of maximum intensity have been chosen. At the highest frequencies (blue contours) the radio source overlies AR 10955, and has apparently two components. The western component of the high-frequency source and the sources at lower frequencies appear to be related to the preceding part of the AR.

The comparison with the days before and after 12 May confirms that the noise storm is in its decay phase on that day. It was brighter, and seen at all NRH frequencies, during the previous two days. The noise storm of 11 May is shown on top of the Hinode/XRT image in the left panel of Fig. 6 at a 50% contour level. It is located in the same region as the noise storm on 12 May, but is brighter. A similar source configuration, with a noise storm that clearly dominates the quiet coronal emission, is observed on 10 May (not shown). On the morning of 13 May, the noise storm was no longer observed by NRH. A new noise storm starts in the western hemisphere at 242 and 327 MHz between 10 and 11 UT, and possibly extends to bursty emission at 151 MHz around 14 UT. As shown in the right panel of Fig. 6, the sources at 327 (green contour) and 237 MHz (yellow contour) come from the same region in the preceding part of AR 10955 as the noise storm of 11 and 12 May. This new emission is therefore probably a revival of the previous noise storm. As in the case described in Sect. 3.1, the Nançay Decameter Array showed recurrent type III bursts and groups of type III bursts at frequencies below 100 MHz.

4.2. Multi-wavelength observations

Figure 7 shows a combination of various observations of AR 10955 on 12 May, which was a mainly bipolar and compact region. As in all ARs, loops connecting the main magnetic polarities are ubiquitous. Large-scale cooler loops are clearly seen in EIS Fe VIII and in TRACE 171 Å emission (0.6–1 MK), while "hot" compact emission is seen in EIS Fe XVI and in the X-rays (XRT). Strong, spatially expanding blue-shifted emission is present on the eastern (following) polarity. Figure 8 shows AR 10955 from 11 to 14 May in Fe XII monochromatic images and Dopplermaps. The stronger blueshifts are persistent, while smaller and more localised blue-shifted emission is present on the western polarity on 11 and 12 May.

4.3. Magnetic field topology

The magnetic field extrapolation of AR 10955 and its surroundings was performed by employing SOHO/MDI magnetic data from 12 May 2007. The field was calculated up to $H = 1\ R_\odot$ using a SOHO/MDI FOV of $L_x \times L_y = 1210'' \times 840''$, embedded in a $D = 900$ Mm $\times$ 900 Mm zero field region. Here we used a smaller D than for AR 10961, since we had to perform a lfff extrapolation with a relatively high value of α, as explained below.

For all α values we tested, the resulting coronal field contained two topologically stable null points: one located at high altitude, above the AR (hereafter NP 1), and a second one located at lower altitude (hereafter NP 2), above the small northern ephemeral region (ER) which displayed a simple bipolar magnetic pattern. However, although the photospheric mapping of separatrix field lines emanating from NP 1 was robust to α changes (in particular, its fan separatrix surface always fully enclosed the AR), the photospheric footpoint of the singular spine field line of NP 2 varied strongly with α: it was located at the western edge of AR 10955 only for strong positive α values.

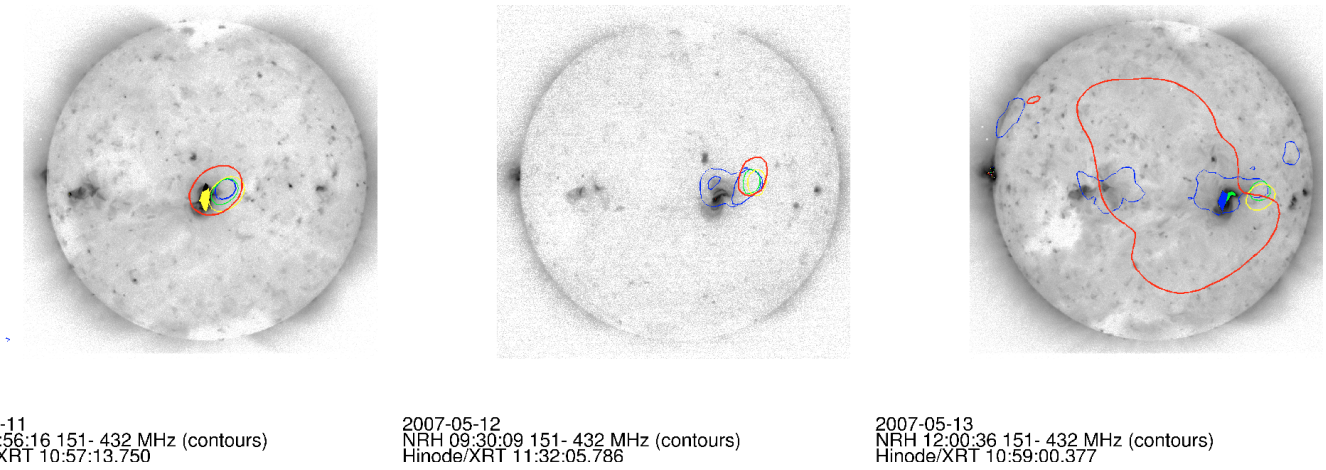

Fig. 6. Hinode XRT (negative) images of AR 10955, superimposed with the brightest radio sources on 11 May 2007 (*left*; iso-intensity contours at 50% of the maximum, 1 min integration), May 12 (*centre*; iso-intensity contours at 80% maximum, 1 min integration) and May 13 (*right*; iso-intensity contours at 80% of the maximum, 5 min integration time). The radio emission comes from a noise storm at all frequencies on 11 May, from the same, decaying noise storm on 12 May, and from a newly emerging noise storm at frequencies down to 237 MHz on 13 May. The large red contour on 13 May shows quiet coronal emission. The noise storm did not extend to this low frequency at the time chosen for the plot. The colours show the same frequencies as in Fig. 2.

If α was decreased, the footpoint successively moved away from the AR, and the spine was even transformed into an open field line. Guided by the S-shaped coronal loops inside AR 10955 and by the faint loops connecting it with the ER (see Fig. 7), taking into account the hemispheric helicity rules for ARs for the latter, we finally used $\alpha = 6 \times 10^{-3}$ Mm^{-1} $\simeq 0.8\alpha_M$ for our analysis presented here.

Figures 9b,c show the magnetic field topology around AR 10955 resulting from the lfff extrapolation. NP 1 is located high above the AR. Its fan surface (pink field lines) fully surrounds the AR, with some of its photospheric footpoints located close to the AR's eastern edge. The fan contains a noticeable twist, which is a consequence of the well-known sensitivity of large-scale structures to α. The twist is probably an artifact of the lfff approximation, and it does not significantly change the overall shape of the fan with respect to a potential field extrapolation. The spine field line related to the fan (also drawn in pink) is rooted in the western edge of the main negative AR polarity below the fan, and is open above it. All field lines surrounding the fan and spine field lines are open as well (drawn in cyan and marked as CH E and CH W). The large-scale topology hence corresponds to the classical open-spine configuration (see, e.g., Pariat et al. 2009).

The open section of the NP 1 spine field line is located above, and to the west, of AR 10955, which corresponds to the location of the brightest source of the radio noise storm (see Fig. 6).

NP 2 is located at a much lower altitude, above the ER. While its fan (drawn in red in Figs. 9b,c) significantly extends away from the ER towards the south-east, it is rooted at the edge of the ER's main positive polarity. With our choice of $\alpha = 6 \times 10^{-3}$ Mm^{-1}, the footpoint of the spine of NP 2 inside AR 10955 is located very close to the photospheric footpoint of the spine of NP 1.

4.4. Interchange reconnection

As done in the previous section for AR 10961, we argue also here that the gradual expansion of AR 10955 leads to a bulging of its outer field lines (drawn in yellow [resp. green] in Figs. 9b,c and d), and to their continuous reconnection across the existing separatrices. Given the geometry of the magnetic field that results from the lfff extrapolation, these field lines should reconnect with the CH W open field lines, which are rooted far to the west of the AR (drawn in blue in Figs. 9d), thus forming new open CH E field lines, rooted at the eastern edge of the AR (drawn in pink in Fig. 9d), as well as new closed connections between the main negative polarity of the AR and the quiet Sun region to the west (drawn in red in Fig. 9d). Such reconnections are of the interchange type, as they involve open field lines.

The photospheric footpoints of these two newly reconnected loops systems roughly correspond to the locations where long-duration blueshifts are observed with EIS (see Figs. 7 and 8). The lack of an exact match between the locations can be attributed to artifacts caused by the lfff approximation; indeed the separatrix of the null point 1 is not only rooted in extended weak field regions (i.e. the quiet Sun), but also formed of very long field lines. The exact shape and footpoint positions, of these lines depend (1) on the magnitude of the weak quiet Sun background positive field, and (2) on the distribution of electric currents in the corona. Regarding the dependence (1), the surface covered by the footpoint of the fan surface is determined such that the magnetic flux in the (a priori well measured) strong field leading negative polarity of the active region is balanced by the positive flux enclosed by the fan surface. Since the fan surface covers an area being much larger than the surface covered by AR 10955, one thus sees that decreasing (resp. increasing) the magnetic fields in the quiet Sun will make the fan footpoints shift farther away from (resp. closer to) the core of AR 10955. This issue may not negligible with MDI's uncertainties in weak field regions. The dependence (2) is even more difficult to quantify, since it would require non-linear force-free extrapolations, motivated by the observed magnetic shear of the XRT loops rooted in the strong fields of AR 10955. It is conservative to argue that the inclusion of a non-uniform large-scale twist, in the long separatrix field lines, will cause their footpoints to shift in the photosphere. Indeed, varying the constant force-free paramater α in our linear force-free field extrapolations (see Sect. 2.3) already results in separatrix shifts of several tens of Mm at several places in the weak field quiet Sun regions. Note that these two limitations are less severe for

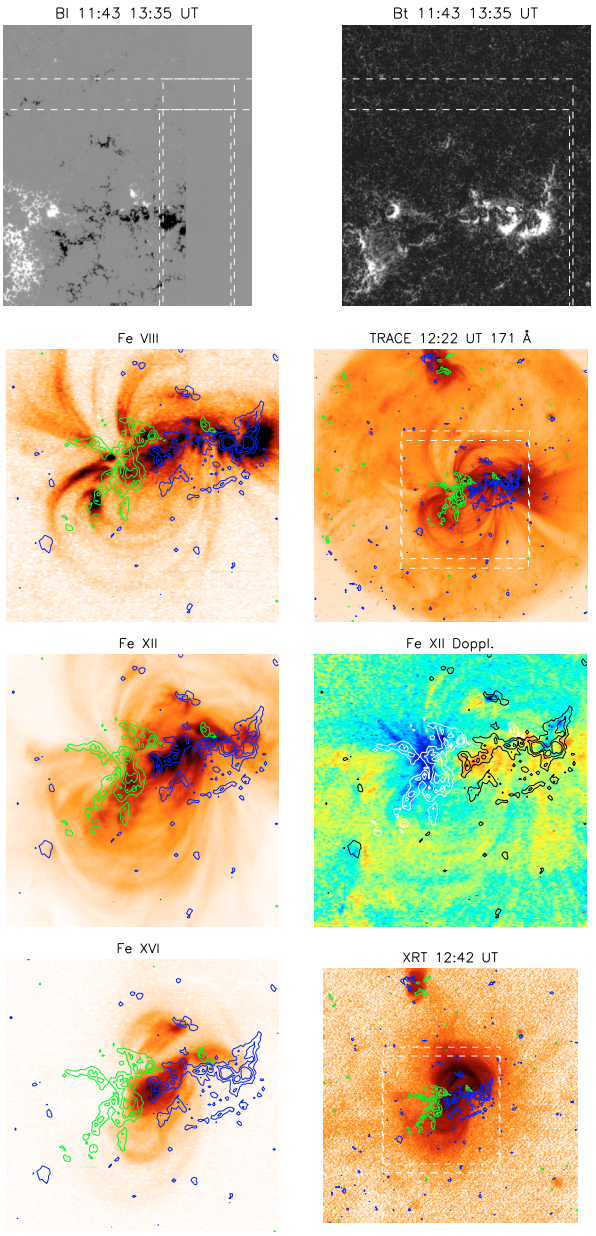

Fig. 7. AR 10955 on 2007 May 12. *Top to bottom*: longitudinal (±800 Gauss) and transverse (±500 Gauss) apparent magnetic field from SOT/SP; "cool" emission as seen in EIS Fe VIII and TRACE 171 Å; 1 MK emission as seen in EIS Fe XII and associated Doppler-map (±20 km s^{-1}); "hot" emission as seen in EIS Fe XVI and in XRT. The FOV of the EIS raster is shown as dashed box in the TRACE and XRT images. Contours superimposed on the images are LOS magnetic field densities from SOHO/MDI.

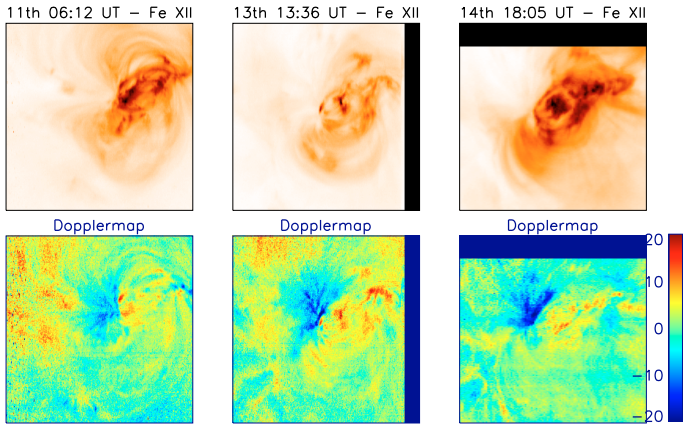

Fig. 8. AR 10955 from the 11th to the 14th May 2007 seen in Fe XII monochromatic images (negative) and Dopplermaps (±20 km s^{-1}).

the other region studied in this paper, AR 10961. Indeed, this region is nicely reproduced by a potential field extrapolation, indicating that its large-scale electric currents are weak, and also its separatrix footpoints (at least those being associated with coronal flows) are all rooted in sunspot and plage regions, where the magnetic field is stronger that in the quiet Sun.

The connections between AR 10955 and the ER are also suitable for magnetic reconnection between closed field lines, across the separatrix that emanates from NP 2. There, AR loops can reconnect with small bipolar arcades (drawn in blue in Fig. 9d), resulting in the formation of (pink and red) connections between the two regions. Even though these connections can be seen as faint loops with XRT, no obvious blue-shifts at the footpoints of these new loops are seen in the EIS data.

One the one hand, it is possible that some blue-shifts associated with reconnection at NP 2 exist, but are not seen by EIS due to its limited FOV. On the other hand, it is possible that the lack of observed blue-shifts associated with the AR-ER magnetic connections shows that magnetic reconnection between two initially bright, and therefore dense, loop systems can not produce strong upflows. The latter explanation would be consistent with the absence of blue-shifts at the northern edge and southern part of the AR 10961 plage, where only closed field lines (i.e. dense loops) could be involved in reconnection. The absence of any bright NRH radio source above the ER does unfortunately not allow to draw a clear conclusion about the presence or absence of AR-ER reconnection (and related blue-shifts), since this reconnection involves only field lines at low altitudes, along which the characteristic plasma frequency is probably too large to be observable with NRH.

5. Discussion and conclusions

By means of multi-wavelength observations and potential (as well as linear force-free) field extrapolations of the coronal magnetic field above and around two quiescent solar ARs, we have studied the relationship between EUV blue-shifts (measured with HINODE/EIS), radio noise storms in the metric domain (recorded by NRH), and high-altitude magnetic reconnection across separatrix surfaces that separate closed magnetic loops from open flux tubes. Our results lead us to propose a unified interpretation for low-altitude coronal outflows emanating from active regions, and radio noise storms located high in the corona, which is summarized in Fig. 10, and discussed in detail below.

Our analyses and results follow on and extend those of Baker et al. (2009): we present several arguments which tend to reduce their list of possible reconnection-related explanations for coronal outflows to the "pressure-driven" case only, which we argue should occur by means of a rarefaction wave. Furthermore, our use of large-scale extrapolations permits us to suggest that the observed outflows are associated with interchange reconnection between open and closed field lines, which Baker et al. (2009) could not firmly show with their extrapolations, due to the smaller computational boxes they used. Finally, we link the coronal outflows to large-scale open separatrix field lines and

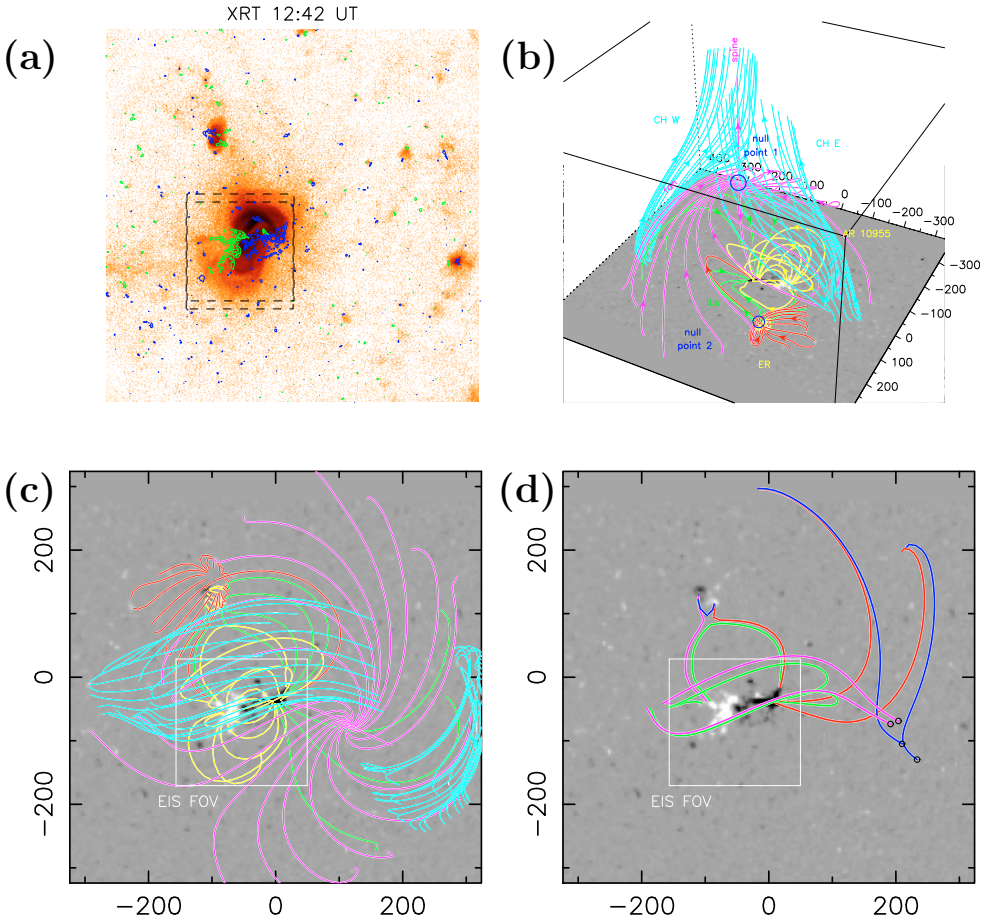

Fig. 9. **a)** X-ray (negative) image from Hinode/XRT of AR 10955 on 12 May 2007. The FOVs of the two EIS channels are shown by dashed boxes. **b–c)** Perspective and top view on selected field magnetic lines from the potential field extrapolation of the AR, outlining its main topological features (see text for details). **d)** Top view on selected field lines from the extrapolation, outlining the interchange reconnection between closed and open field lines (see text for details). Open field lines are marked with a circle where they leave the computational box. The Hinode/EIS FOV is indicated in **c)** and **d)**.

radio noise storms, which are known to be persistent and to map electron beams propagating in the high corona, far above ARs.

5.1. Persistent high-altitude null-point reconnection

The magnetic field extrapolations and the coronal spectroscopy results imply that dense loops in the core of both ARs studied in this paper can continuously reconnect with remote open field lines ("CH regions"). This interchange reconnection takes place at a coronal null point which, according to the extrapolations, is in both cases located high in the corona, more than 100 Mm above the photosphere.

It can be expected that the reconnection is continuous, since ARs are known to expand during their whole lifetime (see, e.g., Zwaan 1985). This interchange reconnection is expected to produce two new loop systems rooted in the AR: one that is open to the heliosphere and one that has a remote connection to the photosphere. Such a reconnection between open and closed fields requires the existence of true separatrices with discontinuous magnetic field connectivities. Note that the occurrence of QSLs (as proposed by Baker et al. 2009) is not excluded from this picture, if one considers them as being "QSL halos" surrounding the separatrices (the existence of which was discovered by Masson et al. 2009).

5.2. Rarefaction-wave-driven outflows in reconnected loops

The first key consequence of the interchange reconnection is that the reconnected loops should be in strong thermal pressure imbalance. The densities of the reconnecting AR and CH field lines differ by one or two orders of magnitude. After reconnection, the sections belonging to the former AR field lines should have a much higher density, and therefore pressure, than the sections belonging to the former CH field lines. As a consequence, a rarefaction wave should be launched from the density gradient located at high altitude, around the former location of reconnection, and travel at the coronal sound speed along the magnetic field in both directions, eventually leading to a gradual transfer of mass from the low-altitude AR portion of a loop to its outer portion, thus triggering mass and momentum exchange. As the AR field continually presses against, and reconnects at, the null point, this shall lead to persistent coronal outflows from the AR footpoints of the reconnecting field lines.

This is exactly what is observed with EIS. Even though our analysis cannot predict the magnitude of the plasma velocity in the outflows with this *rarefaction wave model*, and even though our magnetic field extrapolations were performed in the potential and linear force-free field approximations, a remarkably good correspondence was obtained between the locations of the observed coronal outflows and those of the lower AR portions of the coronal field lines that can be formed by interchange reconnection at the high-altitude null point.

Note that, for both ARs studied here, our extrapolations yielded also closed, low-lying AR (and ER) loops between which reconnection could take place as well. However, we did not observe EUV blue-shifts at the footpoints of these loops. Indeed, since all these loops can be expected to be far denser than flux tubes rooted in open field regions, the pressure imbalance, and therefore the amplitude of the associated rarefaction wave, resulting from reconnection between them should be relatively weak, so significant outflows should not be expected.

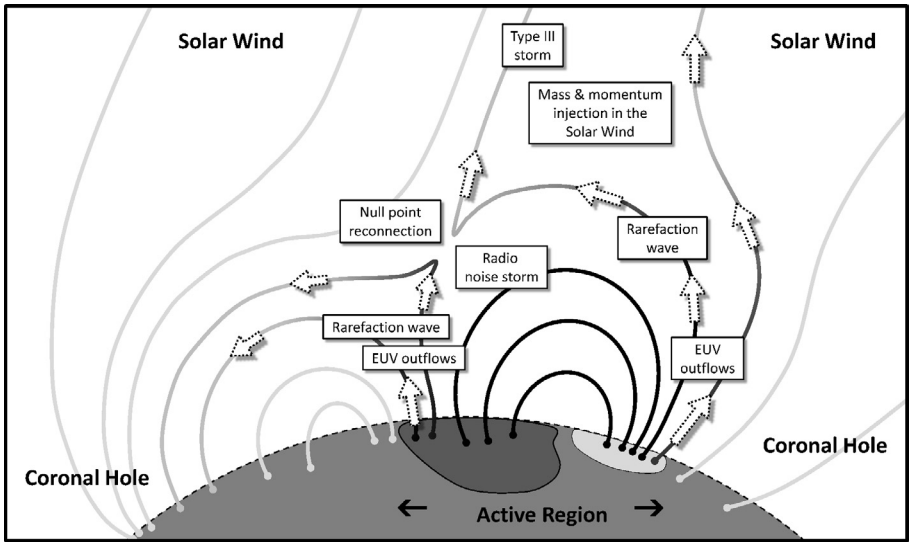

Fig. 10. Summary of our unified interpretation for persistent EUV coronal outflows, radio noise storms, and sporadic weak type III radio emissions. It involves interchange magnetic reconnection at a high altitude coronal null point, continuously driven by slow active region expansion. The reconnection between dense active region loops (black) and diluted CH field lines (light grey) leads to the formation of new closed and open loops with a density gradient (black fading to grey), along which a rarefaction wave triggers low-altitude coronal flows, and along which low-energy electrons are accelerated from the null point, leading to radio emissions.

5.3. Morphology and origin of outflows

For both studied ARs, the photospheric footpoints of the extrapolated separatrix field lines form a segment within the leading sunspot and at the eastern edge of the trailing plage. These calculated separatrix footpoints are located at the observed sharp edges of the areas covered by the coronal outflows, inside of which the EUV emission is very weak.

Firstly, this differs from the flux emergence driven outflow model of Murray et al. (2010), which predicts the development of coronal outflows on both sides of an AR, and not within its main flux concentrations (although it can be argued that projection and LOS integration effects may explain this discrepancy between their idealized model and the observations).

Secondly, we argue that this location of the edges of the outflows regions, inside the AR flux concentrations, and right to the edge of the separatrix footpoints, is evidence of a rarefaction wave. Right after reconnection, such a wave would travel from the reconnection region to the upper transition region at the coronal sound speed. For a typical sound speed of 150 km s^{-1}, and for a null point located at an altitude of 100 Mm, this would take 11 min. Therefore, the wave can be expected to quickly lead to a depletion of the coronal plasma at low altitudes, which eventually would be redistributed all along the reconnected field line. The resulting field-aligned upflows should therefore be cospatial with low-density regions, both having a sharp boundary where the separatrix is located.

Theoretically, this scenario has to be quantified by hydrodynamic simulations which use realistic solar numbers. Observationally, it predicts that the low-altitude portions of the loops that have just reconnected should be less blue-shifted and less diluted than the ones that have reconnected earlier, since the rarefaction wave has not reached for the former altitudes as low as for the latter. This prediction appears to be consistent with the EIS observation of coronal outflows in hot lines described in Sect. 1, but should be further tested with future EIS observations.

Thirdly, it implies that the large horizontal extension of the coronal upflows, as observed in hot lines, should be primarily due to projection effects showing optically thin plasma moving in expanding flux tubes.

5.4. Acceleration of electrons and radio emissions

The second key consequence of the persistent high-altitude interchange reconnection is the continuous acceleration of weakly energetic electrons along the separatrix field lines, in all directions from the reconnection site. Our model cannot estimate the energy of these electrons, although it is qualitatively consistent with low energies, since the magnetic fields which reconnect far above quiescent ARs do not have strong magnetic energy densities.

At the chromospheric heights of the separatrix field lines, low-energy electrons are unlikely to induce significant plasma heating, and therefore are not likely to be the main driver of chromospheric evaporation, as it presumably happens in solar flares (this was one of the possible interpretations for the EUV Dopplershifts proposed by Baker et al. 2009).

At higher altitudes of the same field lines, however, the low-energy electron beams are likely to produce sustained radio emission at the local plasma frequency. Such emissions have indeed been observed in the form of noise storms above both studied ARs. These storms were located exactly at, or very close to, the locations of the high-altitude sections of the separatrix open field lines in our magnetic field extrapolations. The metric noise storms were accompanied by type III storms at longer wavelengths. This demonstrates that electron beams escaped from the acceleration region to the high corona.

5.5. Mass and momentum injection into the solar wind

One of the two field lines that result from an interchange reconnection is obviously open to the heliosphere. It follows that, just like for electrons accelerated at the reconnection site, a fraction of the plasma that is accelerated at low heights by the traveling rarefaction wave can be injected into the interplanetary medium.

Owing to the geometry of the reconnection, only one of the two blue-shifted areas located on either side of ARs should therefore contribute to mass and momentum injection into the solar wind. The plasma flowing out from the other blue-shifted area should only be redistributed all along the closed reconnected loops (see Fig. 10).

The model therefore predicts a direct relation between steady interplanetary density and/or momentum excess (as measurable in-situ, for example) along a given flux tube in the solar wind and the location of EUV outflow regions on one side of an AR in

the Suns lower corona. This prediction could be tested by means of potential field source surface extrapolations or global heliospheric MHD simulations, the calculated field lines of which could be used to check on the occurrence, or lack of, magnetic connections between the low-corona AR outflow regions and the heliospheric steady excess of mass/momentum. This would be a follow-up to previously identified relationships between dense slow solar wind streamers (seen with radio scintillation and with SOHO/LASCO), higher heliospheric Oxygen charge states (measured with ACE and ULYSSES), and dark AR-related EUV emissions at the footpoints of open flux tubes (Kojima et al. 1999; Liewer et al. 2001, 2004). A relationship between an active region and the solar wind was also found by Janardhan et al. (2008). In that case, very low solar wind densities were observed, and related to ongoing interchange reconnection between the active region and a nearby coronal hole.

While the coronal outflows studied in this paper clearly constitute a possible mechanism for developing density and velocity inhomogeneities in the solar wind, without invoking local plasma physic effects, their role in the global acceleration of the solar wind remains to be analysed.

Acknowledgements. GDZ acknowledges support by STFC (UK) through the Advanced Fellowship program. The research leading to these results has received funding from the European Commission's Seventh Framework Programme (FP7/2007-2013) under the grant agreement n 218816 (SOTERIA project, http://www.soteria-space.eu). Financial support by the European Commission through the SOLAIRE network (MTRM-CT-2006-035484) is gratefully acknowledged. The Nançay Radio Observatory is funded by the French Ministry of Education, the CNRS and the Région Centre. Hinode is a Japanese mission developed and launched by ISAS/JAXA, with NAOJ as domestic partner and NASA and STFC (UK) as international partners. It is operated by these agencies in co-operation with ESA and NSC (Norway). We acknowledge use of the Radio monitoring web page, generated and maintained at Observatoire de Paris by LESIA/UMR CNRS 8109 in cooperation with the Artemis team, Universities of Athens and Ioannina and the Naval Research Laboratory. We thank the anonymous referee for useful comments.

References

Alissandrakis, C. E. 1981, A&A, 100, 197
Baker, D., van Driel-Gesztelyi, L., Mandrini, C. H., Démoulin, P., & Murray, M. J. 2009, ApJ, 705, 926
Bentley, R. D., Klein, K.-L., van Driel-Gesztelyi, L., et al. 2000, Sol. Phys., 193, 227
Brueckner, G. E. 1981, in Solar Active Regions: a monograph from Skylab Solar Workshop III, ed. F. Q. Orrall, 113
Bryans, P., Young, P. R., & Doschek, G. A. 2010, ApJ, 715, 1012
Brynildsen, N., Brekke, P., Fredvik, T., et al. 1998, Sol. Phys., 179, 279
Culhane, J. L., Harra, L. K., James, A. M., et al. 2007, Sol. Phys., 60
De Pontieu, B., McIntosh, S. W., Hansteen, V. H., & Schrijver, C. J. 2009, ApJ, 701, L1
Del Zanna, G. 2007, in ASPCS, 397, First Science results from Hinode, 87
Del Zanna, G. 2008a, A&A, 481, L69
Del Zanna, G. 2008b, A&A, 481, L49
Del Zanna, G., & Bradshaw, S. J. 2009, 264
Del Zanna, G., & Mason, H. E. 2003, A&A, 406, 1089
Del Zanna, G., Mason, H. E., & Cirtain, J. 2006, in ESA SP, 617, SOHO-17, 10 Years of SOHO and Beyond
Demoulin, P., Henoux, J. C., Priest, E. R., & Mandrini, C. H. 1996, A&A, 308, 643
Doschek, G. A., Warren, H. P., Mariska, J. T., et al. 2008, ApJ, 686, 1362
Elgarøy, E. Ø. 1977, Solar noise storms (Oxford, Great Britain: Pergamon Press)
Golub, L., Deluca, E., Austin, G., et al. 2007, Sol. Phys., 243, 63
Gurman, J. B., & Athay, R. G. 1983, ApJ, 273, 374
Hara, H., Watanabe, T., Harra, L. K., et al. 2008, ApJ, 678, L67
Harra, L. K., Sakao, T., Mandrini, C. H., et al. 2008, ApJ, 676, L147
Haugan, S. V. H. 1997, SOHO CDS software note, 47
Janardhan, P., Tripathi, D., & Mason, H. E. 2008, A&A, 488, L1
Kai, K., Melrose, D. B., & Suzuki, S. 1985, in Solar Radiophysics: Studies of Emission from the Sun at Metre Wavelengths, ed. D. McLean, & N. Labrum (Cambridge, Great Britain: Cambridge University Press), 415
Kamio, S., Hara, H., Watanabe, T., Fredvik, T., & Hansteen, V. H. 2010, Sol. Phys., 266, 209
Kayser, S. E., Bougeret, J., Fainberg, J., & Stone, R. G. 1987, Sol. Phys., 109, 107
Kerdraon, A., & Delouis, J.-M. 1997, in Lecture Notes in Physics (Berlin Springer Verlag), 483, Coronal Physics from Radio and Space Observations, ed. G. Trottet, 192
Kerdraon, A., & Mercier, C. 1983, A&A, 127, 132
Klein, K.-L. 1998, in Three-Dimensional Structure of Solar Active Regions, ed. C. E. Alissandrakis, & B. Schmieder, ASP Conf. Ser., 155, 182
Kojima, M., Fujiki, K., Ohmi, T., et al. 1999, J. Geophys. Res., 104, 16993
Krucker, S., Benz, A. O., Aschwanden, M. J., & Bastian, T. S. 1995, Sol. Phys., 160, 151
Lecacheux, A. 2000, in AGU Monograph, Radio Astronomy at Long Wavelengths, ed. R. Stone, K. Weiler, M. Goldstein, & J.-L. Bougeret, 119, 321
Liewer, P. C., Hall, J. R., De Jong, M., et al. 2001, J. Geophys. Res., 106, 15903
Liewer, P. C., Neugebauer, M., & Zurbuchen, T. 2004, Sol. Phys., 223, 209
Malik, R. K., & Mercier, C. 1996, Sol. Phys., 165, 347
Marsch, E., Wiegelmann, T., & Xia, L. D. 2004, A&A, 428, 629
Marsch, E., Tian, H., Sun, J., Curdt, W., & Wiegelmann, T. 2008, ApJ, 685, 1262
Masson, S., Pariat, E., Aulanier, G., & Schrijver, C. J. 2009, ApJ, 700, 559
Murray, M. J., Baker, D., van Driel-Gesztelyi, L., & Sun, J. 2010, Sol. Phys., 261, 253
Pariat, E., Antiochos, S. K., & DeVore, C. R. 2009, ApJ, 691, 61
Peter, H. 2010, A&A, 521, A51
Priest, E. R., Bungey, T. N., & Titov, V. S. 1997, Geophys. Astrophys. Fluid Dyn., 84, 127
Raulin, J. P., & Klein, K.-L. 1994, A&A, 281, 536
Schrijver, C. J., Title, A. M., Berger, T. E., et al. 1999, Sol. Phys., 187, 261
Stewart, R. T., Brueckner, G. E., & Dere, K. P. 1986, Sol. Phys., 106, 107
Subramanian, P., & Becker, P. A. 2004, Sol. Phys., 225, 91
Willson, R. F. 2005, Sol. Phys., 227, 311
Winebarger, A. R., DeLuca, E. E., & Golub, L. 2001, ApJ, 553, L81
Winebarger, A. R., Warren, H., van Ballegooijen, A., DeLuca, E. E., & Golub, L. 2002, ApJ, 567, L89
Zwaan, C. 1985, Sol. Phys., 100, 397